A&A 541, A149 (2012)
DOI: 10.1051/0004-6361/201117460

Astronomy & Astrophysics

Transiting exoplanets from the CoRoT space mission

XXII. CoRoT-16b: a hot Jupiter with a hint of eccentricity around a faint solar-like star⋆,⋆⋆

M. Ollivier[1], M. Gillon[2], A. Santerne[3], G. Wuchterl[4], M. Havel[5], H. Bruntt[6], P. Bordé[1], T. Pasternacki[7], M. Endl[8], D. Gandolfi[4,9], S. Aigrain[10], J. M. Almenara[3,11,12], R. Alonso[13], M. Auvergne[14], A. Baglin[14], P. Barge[3], A. S. Bonomo[3], F. Bouchy[15,16], J. Cabrera[7], L. Carone[17], S. Carpano[9], C. Cavarroc[1], W. D. Cochran[8], Sz. Csizmadia[7], H. J. Deeg[11,12], M. Deleuil[3], R. F. Diaz[3], R. Dvorak[18], A. Erikson[7], S. Ferraz-Mello[19], M. Fridlund[9], J.-C. Gazzano[5], S. Grziwa[17], E. Guenther[4], T. Guillot[5], P. Guterman[3], A. Hatzes[4], G. Hébrard[15], H. Lammer[20], A. Léger[1], C. Lovis[13], P. J. MacQueen[8], M. Mayor[13], T. Mazeh[21], C. Moutou[3], A. Ofir[21], M. Pätzold[17], D. Queloz[13], H. Rauer[7,22], D. Rouan[14], B. Samuel[14,1], J. Schneider[23], M. Tadeu dos Santos[19], L. Tal-Or[21], B. Tingley[11,12], and J. Weingrill[20]

(Affiliations can be found after the references)

Received 10 June 2011 / Accepted 16 March 2012

ABSTRACT

Aims. We report the discovery of CoRoT-16b, a low density hot jupiter that orbits a faint G5V star (mV = 15.63) in 5.3523 ± 0.0002 days with slight eccentricity. A fit of the data with no a priori assumptions on the orbit leads to an eccentricity of 0.33 ± 0.1. We discuss this value and also derive the mass and radius of the planet.

Methods. We analyse the photometric transit curve of CoRoT-16 given by the CoRoT satellite, and radial velocity data from the HARPS and HIRES spectrometers. A combined analysis using a Markov chain Monte Carlo algorithm is used to get the system parameters.

Results. CoRoT-16b is a 0.535 −0.083/+0.085 M_J, 1.17 −0.14/+0.16 R_J hot Jupiter with a density of 0.44 −0.14/+0.21 g cm^{-3}. Despite its short orbital distance (0.0618 ± 0.0015 AU) and the age of the parent star (6.73 ± 2.8 Gyr), the planet orbit exhibits significantly non-zero eccentricity. This is very uncommon for this type of objects as tidal effects tend to circularise the orbit. This value is discussed taking into account the characteristics of the star and the observation accuracy.

Key words. stars: fundamental parameters – techniques: photometric – techniques: spectroscopic – techniques: radial velocities – planetary systems

1. Introduction

Since the first detections of extrasolar planets in the beginning of 1990s, several programs for the systematic search for these objects have started, mainly based on radial velocity and photometric transit measurements. These programs have led to the discovery of more than 750 new planets of which more than 25% orbit at a distance closer than 0.07 AU from their parent star and with periods shorter than 6 days (http://exoplanet.eu). Because of their proximity to the star, these planets are considered as "hot planets". Their present position within the planetary system is thought to result from the interaction with either other planets of the system, nearby stars, the protoplanetary disk or a combination of all these effets (Papaloizou & Terquem 2006). These interactions lead to an orbital migration within the planetary system that not only brought the planet close to its parent star, but also usually circularised the orbit thanks to a strong tidal effect between star and planet. As a consequence, about 87% of the planets with an orbital period shorter than 6 days have an eccentricity smaller than 0.1, and only 2 of them have an eccentricity bigger than or equal to 0.3. The highest eccentricity is 0.5171 for HD 147506b (HAT-P-2 b), a massive giant planet (8.74 ± 0.26 M_J) around a F8 star (Bakos et al. 2007). Short period eccentric systems are thus very unusual and results certainly from complex evolution processes.

This paper reports the discovery of CoRoT-16b, a hot Jupiter around a G5V star of magnitude mV = 15, 63. A fit of the radial velocity data within a Monte Carlo Markhov chain (MCMC) analysis leads to a value of the orbital eccentricity of 0.33 −0.1/+0.09. This is one of the highest orbital eccentricities found for such a short period object.

The photometric data were obtained by the CoRoT space telescope. CoRoT conducts a survey dedicated to the search extrasolar planets via photometric measurements (Baglin et al. 2006). A detailed description of the mission and the instrument can be found in the pre-launch book (CoRoT 2006). An overview of the global performance of the CoRoT Observatory after the launch and two years of activity can be found in Auvergne et al. (2009).

We first describe the photometric lightcurve and study the potential sources of photometric contamination thanks to high resolution imaging. We then derive the parameters of the parent star from the high resolution spectroscopic data analysis and describe the analysis of the radial velocity data. We show that,

⋆ The CoRoT space mission, launched on December 27, 2006, has been developed and is operated by the CNES with the contribution of Austria, Belgium, Brasil, ESA, Germany, and Spain.

⋆⋆ Observations made with the HARPS spectrograph at ESO La Silla Observatory (HARPS programs 083.C-0186 and 184.C-0639) and the HIRES spectrograph at the Keck Observatory (NASA-Keck programs N035Hr, N143Hr and N095Hr).

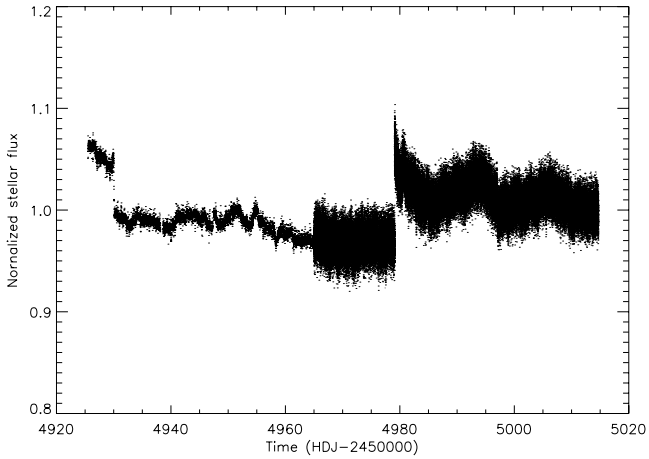

Fig. 1. CoRoT-16 filtered lightcurve.

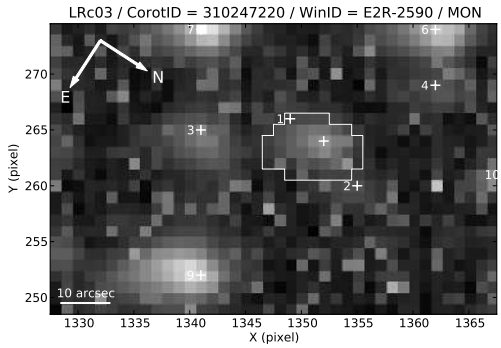

Fig. 2. CoRoT CCD image of the CoRoT-16 target and its environment. No evident bright star appears within the target vicinity.

taking into account the fact that the star is faint, a better estimation of the planetary system parameters can be obtained thanks to a combined MCMC analysis. We finally discuss the planetary orbital parameters and theoretically the structure and evolution of CoRoT-16b.

2. Photometric observations and contamination analysis

2.1. Photometric analysis

The photometric data of LRc03_E2_2590, called later CoRoT-16b (see Table 3 for other denominations) provided by CoRoT consist of 132 124 photometric measurements covering 89.19 days of effective observation from HDJ-2 450 000 = 4925.42 to HDJ-2 450 000 = 5014.61 sampled at a rate of one measurement every 512 s. Starting at HDJ-2 450 000 = 4964.94 the sampling rate was increased to one measurement every 32 s. For brighter stars in the CoRoT exoplanet field prisms provide light curves in three color bands. However, this target was too faint (mV = 15.63) so only white color photometric data exist. It is thus not possible to use the chromatic information to disentangle from complex false positive cases, for instance, involving nearby contaminating stars, eclipsing binaries, etc. other phenomena.

The first step of the photometric analysis consists of a simple filtering of flagged outliers in the lightcurve provided by the CoRoT Data Center (CoRoT 2006). The corresponding filtered lightcurve is shown in Fig. 1. Data were analysed using classical algorithms employed by the CoRoT team since CoRoT-1b (Barge et al. 2008). A signal was identified with a period of 5.3516 ± 0.001 days. Sixteen transit events were identified, starting at HJD-2 450 000 = 4923.9223 ± 0.0089. These were then extracted from the lightcurve and a parabolic fit was performed around each to remove the stellar variability and/or instrumental residuals. Because of the faintness of the star and thus the relatively low signal-to-noise ratio (SNR) of the lightcurve, the photometric lightcurve could not be used independently from the radial velocity data to extract the orbital parameters of the planetary system, particularly the period and the eccentricity.

2.2. Contamination analysis

Figure 2 is a piece of the overall field of CoRoT taken at the beginning of LRc03 (third long run of CoRoT in the galactic center direction), centered around CoRoT-16 target. The shape of the photometric mask is sketched. No evidence of strong contamination appears on that image. The contamination analysis has been performed using the method described in Bordé et al. (2010). Figure 3 from the Palomar Observatory all Sky Survey II (Reid et al. 1991) gives a high angular resolution image of CoRoT-16 and its environment, along with the magnitude of each neighbour. Table 1 gives the coordinates and main characteristics of contaminants as they appear in Fig. 3.

Table 1. Main potential contaminating stars around CoRoT-16 target (#0) and their characteristics.

#	Dist from center (arcsec)	RA J2000 (deg)	Dec J2000 (deg)	mR	Contam. (%)
0	0.000	278.524650	–06.002642	14.9	Target
1	6.733	278.524373	–06.004492	18.6	1.4
2	11.617	278.526698	–06.000139	17.5	0.9
3	24.455	278.526420	–06.009203	14.9	0
4	26.830	278.519845	–05.996923	16.8	0
5	28.810	278.516895	–06.004778	17.7	0
6	33.229	278.516542	–05.998150	13.8	0
7	34.634	278.520167	–06.011167	13.5	0
8	36.144	278.514662	–06.001181	17.3	0
9	37.574	278.533928	–06.007520	13.2	0
10	38.317	278.523509	–05.992059	18.5	0

The contamination level, defined as the ratio of the flux through the photometric mask of all the neighbour stars to the flux of the target itself through the mask, has been estimated to be 2.3% ± 0.8%. The contamination appears to be due to 2 main stars, at respective distances of 6.73 and 11.62 arcsec to CoRoT-16 and with respective R magnitudes of 19.0 and 17.8. Taking into account their distance to the main target and their individual contaminating factor (see Table 1), these should not affect significantly the radial velocity measurements of the target. In addition, only eclipse phenomenon due to the nearest contaminating star (at a level of 1.4%) may be considered as a possible alternative cause for the photometric variation observed on the main target. In order to check this possibility, on-off photometry has been performed using the OGS facility in the Canary Islands, during the nights of 22 October 2009 (on), and 23rd October 2009 (off). These observations show a 1 ± 0.5% deep variation with the right sign on the main target. Nearby stars do not show any relevant variation confirming the hypothesis of a photometric variation on the main target.

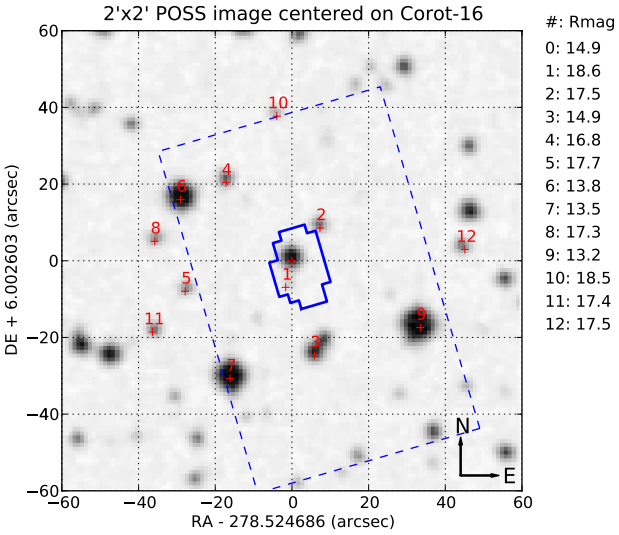

Fig. 3. POSS II image of the CoRoT-16 target and its environment. The contaminants R magnitude is given in the column at the right of the figure. See Table 1 for contamination details.

3. CoRoT-16 stellar parameters

We used the semi-automatic pipeline VWA (Bruntt et al. 2010a,b) to analyse a spectrum of CoRoT-16, obtained with the HIRES spectrograph on Keck. The signal-to-noise ratio in the continuum around 6000 Å is 80. We estimated the profile shape by adjusting $v \sin i$ and macroturbulence of isolated lines and determining the best-fit values of these parameters. We relied on the Fe I and Fe II lines to determine the combination of $T_{\rm eff}$, $\log g$ and microturbulence that minimized the correlation of the abundance of Fe I with equivalent width and excitation potential. We also required that the mean abundance of Fe I and Fe II are the same within the uncertainty. Furthermore, we used the pressure-sensitive calcium lines at 6122 and 6162 Å to constrain $\log g$. This "classical method" of determining fundamental atmospheric parameters has recently been validated by Bruntt et al. (2010a) after analysing several solar-type stars that are "fundamental stars", i.e. stars where $T_{\rm eff}$ and $\log g$ are determined from direct methods, e.g. using interferometry to get $T_{\rm eff}$ and radii and masses for binary systems. They found good agreement between the spectroscopic values using VWA and the values using the direct methods. For CoRoT-16 we determine the parameters given in Table 3. The uncertainties in the parameters were evaluated as described in Bruntt et al. (2010a) and includes systematic errors.

To measure the broadening of the stellar line profiles we used the approach of Bruntt et al. (2010a). We selected 52 isolated lines of Fe, Ni, Ca, Cr and Ti and adjusted the abundance of each line so the observed and computed equivalent widths match. Each line is then convolved by the instrumental spectral resolution of $R = 50\,000$ and a combination of $v \sin i$ and macroturbulence that was varied from 0 to 4 km s^{-1} in steps of 0.5 km s^{-1}. For each of the $9 \times 9 = 81$ different combinations we computed the χ^2 value and the lowest value was chosen as the best fit. We discarded 6 lines with high χ^2 and evaluated the mean value of $v \sin i$ and macroturbulence to be $v \sin i = 0.3$ and $v_{\rm macro} = 1.5$ km s^{-1}. The distribution of measured values are not Gaussian, but we adopt a formal uncertainty of 0.5 km s^{-1} for both broadening parameters. The value of $v_{\rm macro}$ is in agreement with the calibration of Bruntt et al. (2010a) which gives $v_{\rm macro} = 2.1 \pm 0.4$ km s^{-1}. In conclusion, due to the limited resolution of the spectrum, we state that the macroturbulence is typical for the spectral type of the star, $v_{\rm macro} \simeq 2$ km s^{-1}, and $v \sin i$ is certainly below 1 km s^{-1}.

The *Spitzer*/IRAC photometry have also been extracted performing aperture photometry on the 3.6, 4.5, 5.8, and 8.0 μm archival image cut-outs (data tag ADS/IRSA.Atlas#2012/0302/004347_20722) as retrieved from the IRSA-NASA/IPAC Infrared Science Archive[1]. These images are parts of the GLIMPSE survey of the galactic plane (Benjamin et al. 2003). Following the method described in Gandolfi et al. (2008), we used the broad-band photometry reported in Table 3 to derive the interstellar extinction ($A_{\rm V}$) and distance (d) to the star. In Table 3, J, H and Ks photometric data are provided by The Two Micron All Sky Survey (2MASS, Skrutskie et al. 2006). Assuming a normal extinction law and a black body emission at the star's effective temperature and radius, we found $A_{\rm V} = 2.10 \pm 0.10$ mag and $d = 840 \pm 90$ pc. This high extinction is in agreement with the absorption seen in the interstellar Na-D resonance lines, which have zero flux in the stellar spectrum (yielding a lower limit of $A_{\rm V} = 0.6$).

4. Radial velocimetry analysis

We performed radial velocity (RV) observations of CoRoT-16 with the HARPS spectrograph (Pepe et al. 2002b; Mayor et al. 2003), based on the 3.6-m ESO telescope (Chile) and with the HIRES spectrograph based on the 10-m Keck I telescope (Hawaii). 30 HARPS measurements of one hour exposure time on CoRoT-16 were made between August 2009 and August 2010 (ESO programs 083.C-0186 and 184.C-0639) and 7 HIRES measurements of 20-min exposure time were made between June 2009 and August 2010 (Keck programs: N035Hr, N143Hr and N095Hr) as part of the NASA's key science project in support of the CoRoT mission.

HARPS was used with the observing mode obj_AB, without simultaneous thorium calibration. The intrinsic stability of this spectrograph does not require the use of simultaneous thorium calibration, the instrumental drift during one night being in our cases always smaller than the stellar RV photon noise uncertainties. The 5 HARPS first measurements were acquired using the EGGS mode (R(550 nm) $\sim$ 80 000), the others were obtained using the HAM mode (R(550 nm) $\sim$ 110 000). HARPS HAM and EGGS data were reduced with the on-line standard pipeline and radial velocities were obtained by weighted cross-correlation with a numerical G2 mask (Baranne et al. 1996; Pepe et al. 2002a). We quadratically added 30 m s^{-1} to EGGS error bar in order to take in account the ~30 m s^{-1} of systematic errors of this mode. The Moon velocity was always too far from the velocity of CoRoT-16 and never affected the radial velocity measurements. We thus did not need to correct any spectra for Moon scattered light. Because of bad seeing or bad weather conditions, 6 of the 25 HARPS/HAM spectra had too low signal-to-noise ratio ($S/N < 3.5$ per pix. at 550 nm) and were not included in the analysis.

HIRES was used with the red cross-disperser and the I_2-cell to measure the 7 RVs. We used a 0.861″ wide slit that leads to a resolving power of $R \sim 50\,000$. We compute the RVs by differential radial velocities using the *Austral* Doppler code (Endl et al. 2000).

The radial velocities from the HARPS and HIRES spectrographs are given in Table 2 and displayed in Fig. 4. The phase folded radial velocities are shown in Fig. 6 was well as the best fit found from the MCMC analysis (see below). The phase-folded

[1] http://irsa.ipac.caltech.edu/

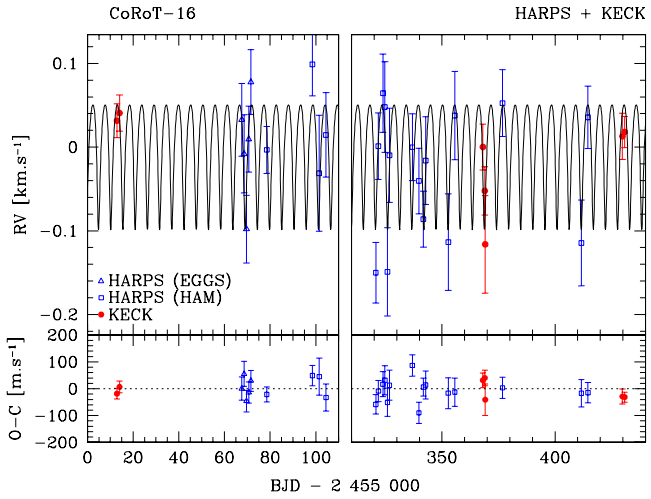

Fig. 4. Radial velocities of CoRoT-16 as function of time.

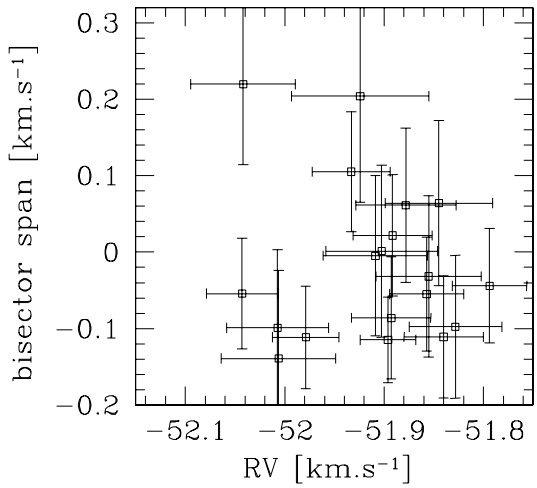

Fig. 5. HARPS-HAM bisector span as function of radial velocity. Bisector error bars are taken as twice the radial velocity uncertainties. No significant slope is visible between radial velocity and bisector, discarding a blend scenario.

radial velocities are clearly in phase with the CoRoT transit consistent with the reflex motion due to a transiting planetary companion on an eccentric orbit. The accurate determination of the system parameters is computed in the framework of the global MCMC analysis that is described in the next section.

In order to examine the possibility that the radial velocity variation is due to a blended binary scenario, we followed the procedure described in Bouchy et al. (2009) which consists in checking the spectral line asymmetries and the dependencies of the RV variations with the cross-correlation mask used. Asymmetries of spectral lines were computed by measuring the bisector span of the CCF and are listed in Table 2 and plotted in Fig. 5. We find a Spearman's rank-order correlation coefficient between radial velocity and bisector of -0.05 ± 0.19 which excludes any significant correlation between them. We also computed the CCF with stellar masks appropriate for F0, G2, and K5 stars. Radial velocity variations caused by a stellar blend or surface spots would show a different amplitude when using the different stellar masks. Once again these did not show any correlation between the template used and the RV amplitude. These two checks tend to exclude that the RV variations are due to a blended binary and confirms the planetary nature of CoRoT-16b.

Table 2. Radial velocity measurements of CoRoT-16 obtained by HARPS and HIRES.

BJD −2 455 000	RV [km s^{-1}]	$\pm1\sigma$ [km s^{-1}]	BIS [km s^{-1}]	Exp. time [s]	S/N/pix. (at 550 nm)
		HARPS – EGGS			
67.60205	–51.9454	0.0434	–0.0365	3400	6.50
68.62368	–51.9861	0.0466	–0.0820	3600	5.90
69.64102	–52.0760	0.0404	0.0089	3300	7.50
70.64996	–51.9685	0.0394	0.0053	3000	7.60
71.58942	–51.9003	0.0388	0.0833	3000	8.00
		HARPS – HAM			
78.56893	–51.8960	0.0281	–0.1148	3600	7.40
98.52473	–51.7939	0.0374	–0.0440	3600	4.60
101.52502	–51.9240	0.0693	0.2041	3600	3.50
104.50018	–51.8781	0.0504	0.0613	3600	4.50
320.76896	–52.0428	0.0361	–0.0543	3600	5.60
321.90436	–51.8916	0.0397	0.0218	3600	5.90
323.90457	–51.8282	0.0467	–0.0977	3600	5.00
324.76683	–51.8449	0.0541	0.0641	3600	3.50
325.90390	–52.0418	0.0527	0.2196	3600	4.00
326.81222	–51.9024	0.0562	0.0012	3600	3.80
336.89012	–51.8928	0.0398	–0.0860	3600	5.30
339.79632	–51.9331	0.0392	0.1051	3600	5.10
341.82049	–51.9788	0.0335	–0.1113	3600	6.20
342.79029	–51.9087	0.0524	–0.0047	3600	4.60
352.78220	–52.0062	0.0576	–0.1392	3600	4.00
355.68523	–51.8551	0.0528	–0.0317	3600	4.20
376.74381	–51.8401	0.0398	–0.1109	3600	5.70
411.64142	–52.0072	0.0512	–0.0989	3600	4.40
414.55156	–51.8571	0.0374	–0.0549	3600	5.10
		HIRES			
12.91010	0.0408	0.0202			
14.03745	0.0500	0.0217			
368.07812	0.0094	0.0274			
368.92843	–0.0430	0.0288			
369.11855	–0.1068	0.0584			
429.77181	0.0222	0.0277			
430.78491	0.0274	0.0186			

Notes. BJD is the barycentric Julian date. 30 m s^{-1} was quadratically added to EGGS errors.

5. Coupled radial velocimetry/photometric analysis

To get the strongest constraints on the system and realistic values and associated errors for its parameters, we performed a global analysis of the CoRoT transit photometry and the HARPS/HIRES RVs. First, we extracted the parts of the CoRoT lightcurve located within 0.15 days of the inferior conjunctions deduced from the preliminary transit ephemeris determined in Sect. 2.1 and obtained 16 individual transit lightcurves. The over-sampled transit lightcurves were binned on 2-min intervals to expedite our analysis. The resulting folded lightcurve (Fig. 6) is still very well sampled.

The global analysis was performed with the Bayesian MCMC algorithm mentioned in the CoRoT-12b discovery paper (Gillon et al. 2010), and we refer the reader to that paper for details.

We performed a first Markov chain to estimate the level of correlated noise in each lightcurve and to scale respectively the photometric error bars. The third and eight transits showed a much larger level of correlated noise than the other transits, and we decided to discard them from the rest of our analysis.

The jump parameters of the MCMC were: the planet/star area ratio $(R_p/R_s)^2$, the transit width (from first to last contact) W, the parameter $b' = a\cos i/R_*$ (which is the transit impact

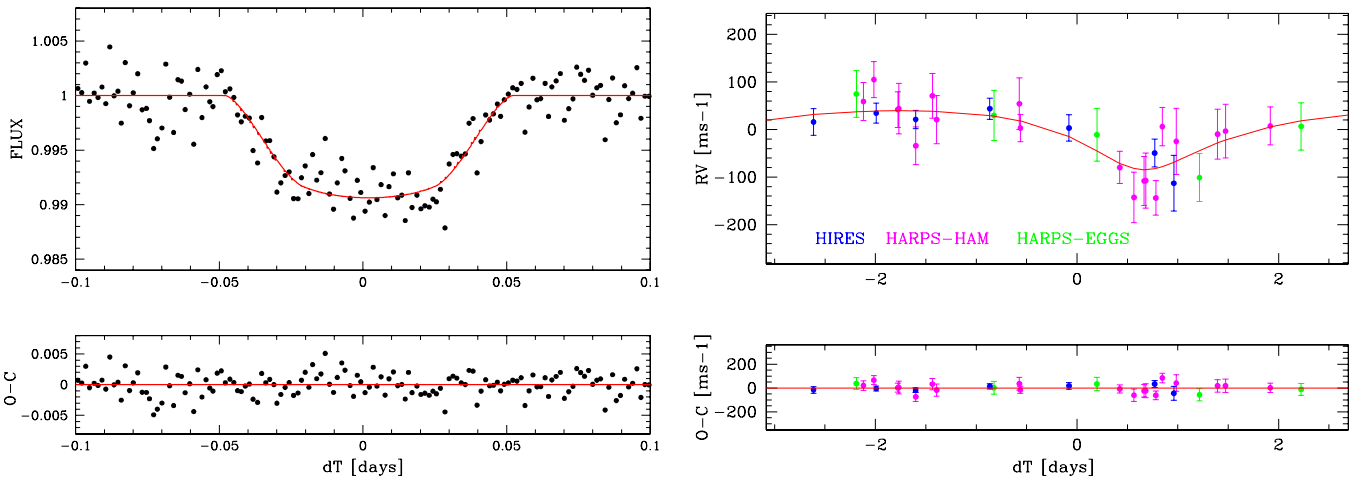

Fig. 6. Result from the MCMC combined analysis: (*left*) phase folded photometric lightcurve and best fit of the transit and residuals, (*right*) phase folded radial velocity curve, best fit and residuals.

parameter in the case of a circular orbit), the orbital period P and time of minimum light T_0, the two parameters $\sqrt{e}\cos\omega$ and $\sqrt{e}\sin\omega$ where e is the orbital eccentricity and ω is the argument of periastron, and the parameter $K_2 = K\sqrt{1-e^2}\,P^{1/3}$, where K is the RV orbital semi-amplitude. We assumed a uniform prior distribution for all these jump parameters. To take into account the dilution of the signal due to contaminating stars (see Sect. 2.2), the jump parameters $(R_p/R_s)^2$ was divided at each step of the MCMC by a number drawn from the distribution $N(1.023, 0.008^2)$ before being used in the computation of the eclipse model. We assumed a fourth-order time polynomial as baseline model for each of the 14 CoRoT transit lightcurves. The coefficients of these baseline models were determined by least-square minimization at each of the steps of the Markov chains.

We assumed a quadratic limb-darkening law and we allowed the quadratic coefficients u_1 and u_2 to float in our MCMC runs, using as jump parameters the combinations $c_1 = 2\times u_1 + u_2$ and $c_2 = u_1 - 2\times u_2$. We assumed normal prior distributions for u_1 ($N(0.47, 0.02^2)$) and u_2 ($N(0.21, 0.0115^2)$) based on theoretical values presented by Sing (2010) for the CoRoT non-standard bandpass and for the spectroscopic parameters of CoRoT-16 (see Sect. 3).

As for CoRoT-12b, the stellar density deduced from the jump parameters, and values for $T_{\rm eff}$ and [Fe/H], drawn from the normal distributions deduced from our spectroscopic analysis, were used at each step of the MCMC as input for a modified version of the stellar mass calibration law deduced by Torres et al. (2010) from well-constrained detached binary systems. Using the resulting stellar mass, the physical parameters of the system were then deduced from the jump parameters at each MCMC step. As the eccentricity of the orbit is not well constrained, the uncertainty on the stellar density is very large, translating into large errors on all the system physical parameters. Therefore we decided to use the distribution $N(4.36, 0.10^2)$ resulting from our spectroscopic analysis as prior distribution for the stellar gravity $\log g_*$.

The analysis was composed of two MCMC chains of 500 000 steps, the first 20% of each chain being considered as its burn-in phase and discarded. Table 3 presents the median and $1-\sigma$ limits of the resulting marginalized posterior distributions for the parameters of the system.

6. Blend analysis

We performed photometric blend analysis inspired by the blender software (Torres et al. 2005, 2011). We call "star 1" the primary target, "star 2" the primary component of a blended eclipsing system and "body 3" the secondary component of the blended eclipsing system that can be either a star (star 3) or a planet. We first interpolated the ATLAS9 model atmospheres of Castelli & Kurucz (2004) to the values of the $T_{\rm eff}$, $\log g$ and metallicity, applied an extinction law of Fitzpatrick (1999) to the $E(B-V)$ of the galactic interstellar extinction model of Amôres & Lépine (2005), and finally applied the spectral response function of CoRoT given in Auvergne et al. (2009) to get the observed flux of star 1. Next, we extracted randomly one value for the mass of the star 2 in a range 0.15–3.00 $M_\odot$, and a mass of the body 3 from the planetary range up to the mass of the star 2. We chose a value for the eccentricity and the longitude of the periastron from a normal distribution of the orbital solution from the MCMC analysis. We chose randomly a distance for the blended eclipsing system (from 0 to 20 kpc). The orbital inclination was estimated from the orbital parameters and transit duration, taking into account its error. To get the physical parameters of star 2 and star 3 we interpolated the isochrones of Marigo et al. (2008) and Girardi et al. (2010)[2] using solar metallicity. Their observed fluxes were estimated from model atmospheres, applying an extinction law and the spectral response function of CoRoT as we did for the star 1. To consider the scenario the flux of the blend observed by CoRoT should be less than the flux observed for the star 1. Then we computed the light curve of the blended eclipsing system using the JKTEBOP code (Southworth et al. 2004a,b) based on ebop (Popper & Etzel 1981; Etzel 1981) and the limb-darkening coefficients computed for CoRoT by Sing (2010). We diluted the light-curve of the eclipsing system using the observed flux of star 1 and the flux in the mask from the contaminating stars, and calculated the χ^2 with respect to the CoRoT-16 light curve. In total 1.2×10^8 photometric blend models were computed and compared to the data.

We also performed radial velocity blend analysis by simulating HARPS cross-correlation function (CCF) of star 1 blended by an eclipsing binary composed by star 2 and star 3. To do that, we first calibrated HARPS – HAM CCFs as a function of

[2] http://stev.oapd.inaf.it/cgi-bin/cmd

Table 3. Star and planet characteristics of the CoRoT-16 system.

Stellar parameters	
CoRoT-ID	310247220
CoRoT-WinID	LRc03-E2-2590
2MASS	453255296
USNO-B1	0839-0404147
Coordinates (J2000)	18:34:05.926 –06:00:09.34
Magnitudes B, V, r', i'	16.68, 15.63, 15.54, 14.75
Magnitude J	13.496 ± 0.026 mag
Magnitude H	12.980 ± 0.029 mag
Magnitude Ks	12.847 ± 0.036 mag
Magnitude at 3.6 μm	12.671 ± 0.072 mag
Magnitude at 4.5 μm	12.793 ± 0.102 mag
Magnitude at 5.8 μm	12.662 ± 0.169 mag
Magnitude at 8.0 μm	12.573 ± 0.214 mag
Spectral type	G5V
Effective temperature, $T_{\rm eff}$	5650 ± 100 K
Surface gravity, $\log g$	4.36 ± 0.1 (cgs)
Stellar density, $\rho_\star$	0.93 –0.24/+0.33 g cm^{-3}
$M_\star^{1/3}/R_\star$	0.9 ± 0.1 (solar units)
Metallicity, [M/H]	+0.19 ± 0.06
Micro-turbulent velocity, $v_{\rm mic}$	0.88 ± 0.14 km s^{-1}
Macro-turbulent velocity, $v_{\rm mac}$	1.5 ± 0.5 km s^{-1}
Rotational velocity, $v \sin i$	<1 km s^{-1}
Star mass, $M_\star$	1.098 –0.078/+0.082 $M_\odot$
Star radius, $R_\star$	1.19 –0.13/+0.14 $R_\odot$
Star age	6.73 ± 2.8 Gyr
Stellar extinction A_V	2.10 ± 0.10 mag
Star distance	840 ± 90 pc
Planet and transit parameters	
Planet period, P	5.35227 ± 0.00020 days
Planet mass, $M_{\rm p}$	0.535 –0.083/+0.085 $M_{\rm J}$
Planet radius, $R_{\rm p}$	1.17 –0.14/+0.16 $R_{\rm J}$
Planet density, $\rho_{\rm p}$	0.44 –0.14/+0.21 g cm^{-3}
Planet orbital semi-major axis, a	0.0618 ± 0.0015 AU
Transit epoch, T_0	HJD 2 454 923.9138 –0.0022/+0.0021
Transit duration, T_{14}	2.39 ± 0.09 h
Transit relative depth, δ	(1.020 –0.092/+0.095) ×10^{-2}
Radius ratio, $R_{\rm p}/R_\star$	0.1010 ± 0.0046
Scaled semi-major axis, $a/R_\star$	11.20 –1.09/+1.21
Orbital inclination, i	85.01 –1.20/+0.94 °
Impact parameter, b	0.825 –0.039/+0.030
Radial velocity semi-amplitude, K	61.96 –9.35/+9.47 m s^{-1}
Orbital eccentricity, e	0.33 –0.10/+0.09
Periastron longitude, ω	168.41 –20.93/+22.83
MCMC jump parameter $\sqrt{e}\cos\omega$	–0.53 –0.09/+0.13
MCMC jump parameter $\sqrt{e}\sin\omega$	0.11 ± 0.2

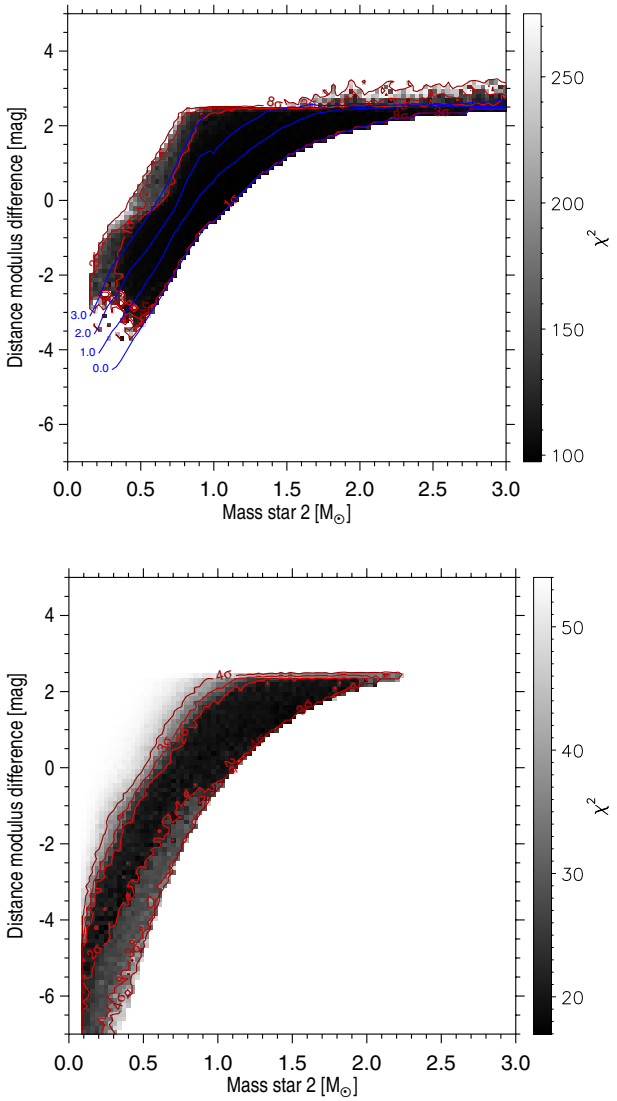

Fig. 7. χ^2 Maps of the blend scenario. *Top panel* represent the photometric χ^2 map with 1-σ, 3-σ and 8-σ contours (red lines). The magnitude difference m_v between the star 1 and star 2 are over-plotted in blue. *Bottom panel* display the radial velocity χ^2 and the 2-σ, 3-σ and 4-σ contours (red lines). Models with a blend system brighter than the target were not considerated.

CCF area (W), the stellar mass (M) and [Fe/H] by analyzing the 24 first CoRoT planet host-stars CCF observed by HARPS – HAM in the same spirit as Boisse et al. (2010). We found for the G2 mask that $\log(W) = 0.870–0.343M/M_\odot + 0.203$[Fe/H] with a quite low dispersion due to the low signal-to-noise of the HARPS – HAM spectra. For the simulations, we assumed that both systems have the same [Fe/H] and we chose randomly the parameters of star 2 and 3, which included $v \sin i$ and masses that was varying in the same ranges than for the photometric blend analysis. We also chose randomly the distance and systemic radial velocity of the blended system that led to a total of 6 free parameters. We fixed the orbital parameters to those derived by the MCMC analysis in order to speed up the simulation. After blending the synthetic CCFs of both stars with respect to the magnitude, bolometric correction and extinction coefficient of each star we measured the resulting radial velocity. We independently computed 5.5 × 10^7 sets of CCF models and compute the χ^2 with respect to the CoRoT-16 HARPS – HAM radial velocity curve. Neither HARPS – EGGS data nor HIRES data were taken into account for this blend analysis since no CCF calibration were computed.

We built the RV and photometric χ^2 maps in the parameter space of mass of star 2, distance modulus (ΔM = 5 log(distance eclipsing system/distance star 1). In each box of the two-dimensional grid, we took the minimum χ^2 of all the blend models inside that box (see Fig. 7). For the best model in each box we computed a χ^2 comparing the combined spectral energy distribution (SED) with the three 2MASS magnitudes and the four *Spitzer*/IRAC data, which are the ones less affected by the extinction, in the way described by Bayo et al. (2008, see Fig. 8). We note that no model is compatible with the data when the distance modulus difference is greater than about 2.5 mag in both RV and light-curve χ^2 maps. This is due to the fact that the extinction rapidly increases at this distance from the target hiding most of the background stars. This extinction wall was one of the main motivation to select this CoRoT exoplanet field (LRc03).

We computed, in the same way as above, the star-with-planet scenario χ^2. Both scenarios are compatible with the RV and

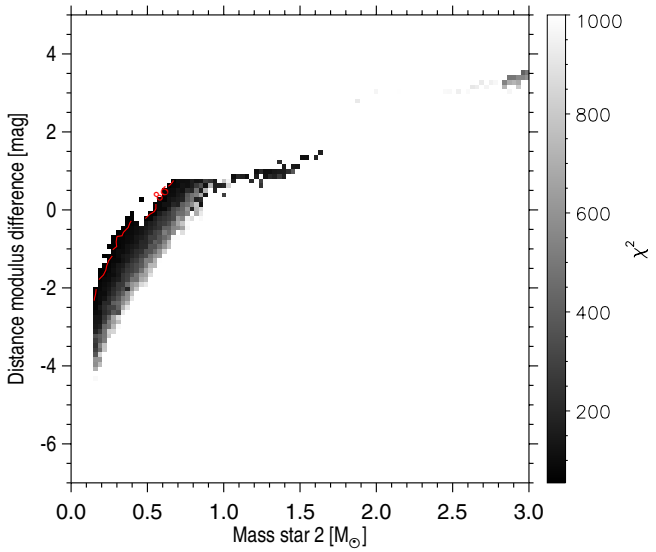

Fig. 8. SED χ^2 maps of the blend scenario. The resulting SED χ^2 is greater than 7-σ.

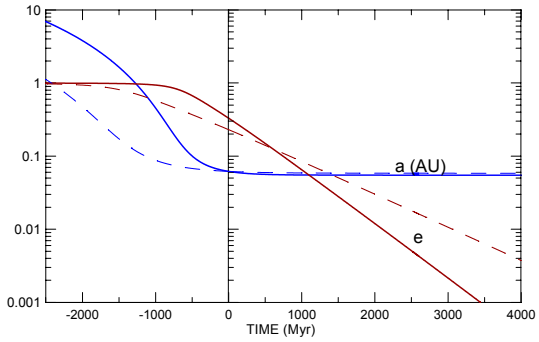

Fig. 9. Tidal evolution of the orbital semi-major axis and eccentricity with the estiated value of the current eccentricity (e = 0.33). The dashed line shows the evolution coresponding to a smaller value (lower bound of the interval of confidence) of current eccentricity (e = 0.23).

light-curve data within 2-σ and 1-σ (respectively). The SED χ^2_r of the star 1 with a planet is 3.2 (3-σ) when its best value for a blend scenario is 19.0 (7-σ). We thus exclude all blend scenarios with a significant level of more than 7-σ.

7. Discussion

7.1. Effective eccentricity of CoRoT-16b

The answer to the question of whether CoRoT-16b has a significant orbital eccentricity is not obvious. The target is faint (mV = 15.63) and the RV observational data exhibit large error bars. In order to check the hypothesis of a highly eccentricity orbit, several analysis have been performed using several hypotheses. The first one, described in the previous section, assumes no a priori assumption on the eccentricity probability distribution. It leads to an orbital eccentricity of 0.33 ± 0.1. An analysis assuming a circular orbit was performed and this led to another set of slightly different parameters. In order to compare the two models, the Bayes factor between the eccentric and circular solutions has been obtained using the Chib & Jeliaskov's method (Chib & Jeliazkov 2001). Its value is 54.1 and may be considered as a strong piece of evidence in favor of the eccentric model (Jeffreys 1961). However, the knowledge of the statistical distribution of the eccentricity within the hot jupiters population, computed thanks to more than one hundred known objects allows us to take this parameter into account as one of the inputs into the MCMC analysis. In that case, the Bayes ratio is only 0.7, which moderates strongly the eccentric solution probability. Finally, if we consider several other models, including a 2 planet model, reasonable fits of the radial velocity data can still be obtained even if no other periodic signal from another transiting planet can be exhibited in the photometric data at the corresponding period. This shows clearly that the S/N ratio of both photometric and radial velocity data does not allow us to reach definitive conclusions. At this level, it is thus not possible to exclude completely a circular orbit for CoRoT-16b, even if the eccentric solution appears, at present, to be the best one. More radial velocity observations would be necessary to make this scenario stronger.

7.2. The tidal history of CoRoT-16b

CoRoT-16b is a hot Jupiter with a mass and distance from the star such that tidal effects may occur, but whose eccentricity has not yet been damped to zero so that the traces of its past evolution have not yet been completely erased. The tidal evolution of the star-planet system has been studied assuming a linear tidal model (Mignard 1979; Hut 1981). In this study, we have adopted, for the central star, the modified quality factor $Q'_s = 10^7$, as found by Hansen (2010) and Benítez-Llambay et al. (2011) from studies of the characteristics of the known systems with hot Jupiters. For the planet, we have derived one value from the actually determined Q' of Jupiter ($Q'_{\rm Jup} = 1.36 \times 10^5$ cf. Lainey et al. 2009) which was transformed into the planets Q'_p, taking into account that: (i) Q'_p scales with the tide forcing period (see Ferraz-Mello et al. 2008); (ii) Q'_p scales with R^{-5} (cf. Eggleton et al. 1998; Ogilvie & Lin 2004). We thus obtain, for CoRoT-16b the factor $Q'_p = 9 \times 10^5$. It is worth mentioning that we have used the linear tidal theory to determine the current rotation period of the planet whose stationary value (3.18 days) is independent of the adopted dissipation parameters. Figure 9 shows the variation of the semi-major axis and eccentricity due to the tidal interaction between the planet and the star for the adopted parameters. It shows circularization about 1 Gyr in the past. The planet rotation is currently in a stationary super-synchronous state and approaches synchronization when the eccentricity tends to zero (Fig. 10). The most critical results are obtained when the past evolution is studied. About 1–2 Gyr before now, the eccentricity would have been very close to 1. The semi-major axis also appears evolving from a very-high value. This behavior is not consistent with the age of the star (6.7 ± 2.8 Gyr). All mechanisms discussed in literature (Malmberg & Davies 2009), as possible explanations for the exoplanets high-eccentricities concern events expected to occur in the early stages of the formation of the system. In order to have compatibility of the various parameters, the current eccentricity should be smaller. Often, the small number of radial velocity observations is responsible for getting initial eccentricity determinations larger than the actual one (Giuppone et al. 2009; Zakamska et al. 2011). However, when transits have been observed, eccentricities are very well constrained. Indeed, in the case of CoRoT-16b, if the eccentricity is not taken into account, the time of the first transit resulting from the radial velocities alone is displaced by several hours. In order to have the right transit time, the true longitude at the minimum of the intensity during the transit must be equal to 90 degrees. The orbit

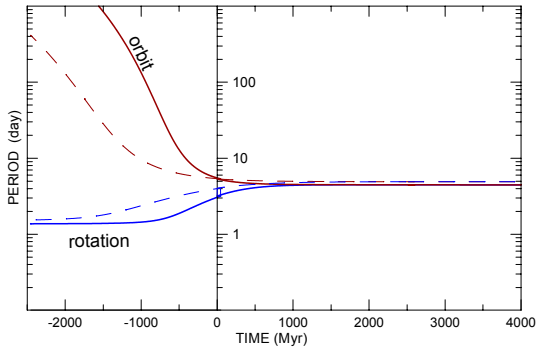

Fig. 10. Tidal evolution of the planetary rotation and orbital periods with the estiated value of the current eccentricity ($e = 0.33$). The dashed line shows the evolution coresponding to a smaller value (lower bound of the interval of confidence) of current eccentricity ($e = 0.23$).

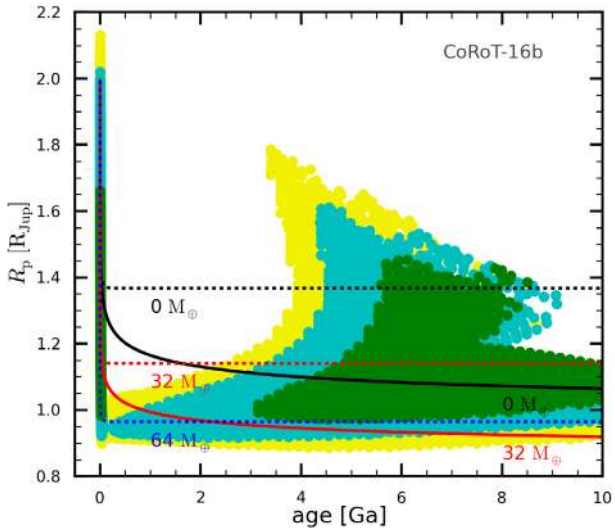

Fig. 11. Constraints obtained on the age (in billions years) and radius of CoRoT-16b (radius in Jupiter units). The colored circles correspond to stellar models solutions that match the inferred $\rho_\star$-$T_{\rm eff}$ uncertainty ellipse within 1σ (green), 2σ (blue), or 3σ (yellow). The evolution tracks show the contraction of a 0.535 $M_{\rm Jup}$ planet with $T_{\rm eq} \sim 1200$ K, in the so-called "standard approach" (plain lines), and when dissipating 0.25% of the incoming stellar flux, or about 2.6×10^{26} erg s^{-1} at the center (dashed lines). The line colors correspond to different masses of the planetary rocky core: 0 $M_\oplus$ (black), 32 $M_\oplus$ (red), and 64 $M_\oplus$ (blue).

determination indicates at the time of the first transit a mean longitude of 111 ± 4 degrees. This difference introduces a strong constraint in the orbit determination which guarantees a a determination of both the eccentricity and the longitude of the pericenter with an accuracy much better than that which is obtained when only radial velocity data are used. In order to conciliate the eccentricity thus obtained for CoRoT-16b and the evolution shown in Fig. 9 we have two possibilities: (i) the age of the star is smaller; (ii) the actual value of $Q'_{\rm pl}$ is larger. Indeed, the time scale of the tidal evolution of this system is almost linearly related to the value of the dissipation in the planet (the star tide is much less efficient in this system than the planetary tide). If a value $Q'_{\rm pl} \sim 10^7$ is adopted, the time scale of Figs. 9 and 10 is multiplied by ∼10 and the past evolution becomes consistent with the age of the star. This value of $Q'_{\rm pl}$ is however much higher than the usually considered values and higher than the corresponding value actually determined for Jupiter. This higher value would be rather comparable to some results of the statistical determination carried out by Hansen (2010) indicating that hot Jupiters have dissipation values mostly in the interval $10^7 < Q'_{\rm pl} < 10^8$. This result strongly depends on the current orbital eccentricity and for this reason, Figs. 9 and 10 show also (dashed line) the evolution which would correspond to the lower bound of the interval of confidence of the present eccentricity ($e = 0.23$).

7.3. Internal structure and evolution of the planet

In order to assess the possible bulk composition of CoRoT-16b, we performed a combined analysis of the star and planet using photometric, spectroscopic, and radial velocity data and their associated error bars. This work has been done using a modeling tool called SET (Stars and Exoplanets modeling Tool, Guillot & Havel 2011; Havel et al. 2011). Figure 11 shows the results for the planetary radius as a function of the age of the star. The colored circles indicate the quality of the fit between stellar evolution models (CESAM, Morel & Lebreton 2008) and the inferred constraints on the stellar mean density, effective temperature and metallicity for less than 1σ (green), 2σ (blue) and 3σ (yellow). We also represent theoretical planetary evolution models (using CEPAM, Guillot & Morel 1995) assuming a total planetary mass of 0.535 $M_{\rm jup}$, a $T_{\rm eq}$ of 1200 K and a different hypotheses: using a "standard model" (plain lines), i.e. without additional sources of heat; by dissipating a fraction (0.25% or about 2.6×10^{26} erg s^{-1}) of the incoming stellar flux in the deep interior of the planet (dashed lines). The latter case is a standard recipe to explain inflated giant planets (Guillot 2008), and may possibly be justified by, for instance, ohmic dissipation (Perna et al. 2010). Depending on the assumption, CoRoT-16b could be a pure H-He planet (black lines), or could contain up to 64 $M_\oplus$ (at 1σ) of heavy elements (blue line). This means that between 0 and ∼38% of the planet's total mass is in the core, a weak constraint compatible with the somehow poorly constrained planetary radius (an uncertainty of 13%) and age. A better determination of the stellar parameters would very likely tighten the contraints on the planetary radius, but is still very difficult because the star is faint.

In our planetary evolutions calculations, we assumed all heavy elements to be grouped into a dense central core, surrounded by a solar-composition envelope. The possibility that these heavy elements may be at least partly mixed in the envelope is not expected to change the results significantly (Guillot 2005; Ikoma et al. 2006; Baraffe et al. 2008).

7.4. CoRoT-16b and theoretical planet statistics

With the significant number of theoretical evolution models consistent with the determined parameters of CoRoT-16b, it is of interest to look how it fits into the statistics of planetary equilibria in the framework of a general theory of planet formation that provides statistics of planets consistent with basic physical principles (Wuchterl 2011). That puts CoRoT-16b into the context of what is physically probable.

Figure 11 shows that coreless planets with radii of 0.95 to 1.4 $R_{\rm Jup}$ are consitent to 1σ with an age of 4–10 Ga and the constraints for the CoRoT-16-system presented here. The combined analysis gives $(M_{\rm p}, R_{\rm p}) = (0.535 \pm 0.085\ M_{\rm J}, 1.17 \pm 0.15\ R_{\rm J})$. For a first synopsis we compare the mass to the high resolution CoRoT-Mark 3 theoretical mass spectra[3] for the case of a G2 star

[3] 2007 Mark 2 online, available at http://www.space.unibe.ch/~broeg

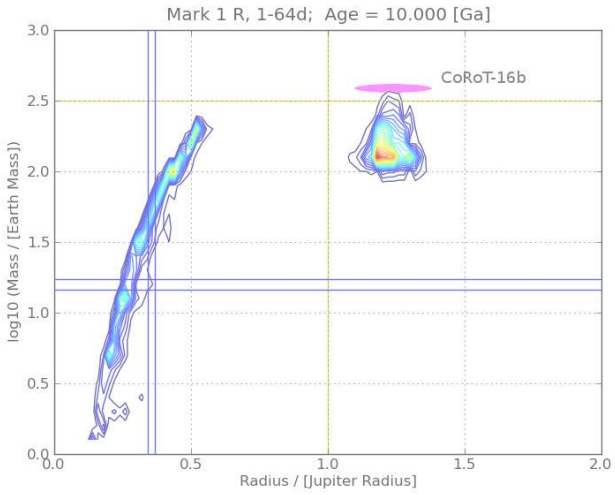

Fig. 12. Probabilistic theoretical mass radius diagram for hypothetical, physically possible planetary equilibria on orbits between 1 d and 64 d around CoRoT-16 at an age of 10 Ga. Coloured contours mark the number density of planetary models. The measured values for CoRoT-16b are indicated by a magenta error-ellipse.

and an orbital period of 5 days (Broeg 2009). The peak in the theoretical mass-distribution is between 0.5 and 2.1 M_J (Broeg 2007). Thus CoRoT-16b's mass is near the high, approximately Jupiter mass peak of the bimodal mass spectra typical for this host star mass and orbital period. Theoretically CoRoT-16b is a likely planet in the sense that many physical configurations exist that lead to this planet mass. 80% of the theoretical planets have smaller mass according to the cumulative the Mark 3 distributions. Accordingly it is a common, somewhat high mass but, not extreme planet for its environment.

From the theoretical mass distributions the radius distributions at any given age can be derived by planetary evolution calculations (Wuchterl 2011). In Fig. 12 we show CoRoT-16b in the probabilistic MRD for an age of 10 Ga. The planet is located towards the high mass end of the theoretical population and within the observational errors the radius overlaps well with the theoretically expected values for the respective Hot Jupiter population in a 5 day orbit around a star like CoRoT-16.

Acknowledgements. We wish to thank the ESO staff for their support and for their contribution to the success of the HARPS project and operation at ESO La Silla Observatory. The French team wish to thank the Programme National de Planétologie (PNP) of CNRS/INSU and the French National Research Agency (ANR-08-JCJC-0102-01) for their continuous support to our planet search program. The team at the IAC acknowledges support by grants ESP2007-65480-C02-02 and AYA2010-20982-C02-02 of the Spanish Ministerio de Ciencia e Innovación. The German CoRoT Team (TLS and the University of Cologne) acknowledges DLR grants 50OW0204, 50O0603, and 50QP07011. M. Gillon is FNRS Research Associate. T. Mazeh acknowledges the supported of the Israeli Science Foundation (grant No. 655/07). M. Endl, W. D. Cochran and P. J. MacQueen were supported by NASA Origins of Solar Systems grant NNX09AB30G. This research has made use of the SIMBAD database, operated at the CDS, Strasbourg, France, and of NASA's Astrophysics Data System. Part of the data presented herein were obtained at the W. M. Keck Observatory from telescope time allocated to the National Aeronautics and Space Administration through the agency's scientific partnership with the California Institute of Technology and the University of California. The Observatory was made possible by the generous financial support of the W. M. Keck Foundation. The contamination analysis using *Spitzer* data has made use of the NASA/ IPAC Infrared Science Archive, which is operated by the Jet Propulsion Laboratory, California Institute of Technology, under contract with the National Aeronautics and Space Administration. Some of the data presented were acquired with ESAs OGS telescope at Teide Observatory of the Instituto de Astrofísica de Canarias.

References

Amôres, E. B., & Lépine, J. R. D. 2005, AJ, 130, 659
Auvergne, M., Bodin, P., Boisnard, L., et al. 2009, A&A, 506, 411
Baglin, A., Auvergne, M., Boisnard, L., et al. 2006, in COSPAR, Plenary Meeting, 36th COSPAR Scientific Assembly, 36, 3749
Bakos, G. Á., Kovács, G., Torres, G., et al. 2007, ApJ, 670, 826
Baraffe, I., Chabrier, G., & Barman, T. 2008, A&A, 482, 315
Baranne, A., Queloz, D., Mayor, M., et al. 1996, A&AS, 119, 373
Barge, P., Baglin, A., Auvergne, M., et al. 2008, A&A, 482, L17
Bayo, A., Rodrigo, C., Barrado, Y., et al. 2008, A&A, 492, 277
Benítez-Llambay, P., Masset, F., & Beaugé, C. 2011, A&A, 528, A2
Benjamin, R. A., Churchwell, E., Babler, B. L., et al. 2003, PASP, 115, 953
Boisse, I., Eggenberger, A., Santos, N. C., et al. 2010, A&A, 523, A88
Bordé, P., Bouchy, F., Deleuil, M., et al. 2010, A&A, 520, A66
Bouchy, F., Moutou, C., Queloz, D., & the CoRoT Exoplanet Science Team 2009, in IAU Symp., 253, 129
Broeg, C. 2007, MNRAS, 377, L44
Broeg, C. H. 2009, Icarus, 204, 15
Bruntt, H., Bedding, T. R., Quirion, P., et al. 2010a, MNRAS, 405, 1907
Bruntt, H., Deleuil, M., Fridlund, M., et al. 2010b, A&A, 519, A51
Castelli, F., & Kurucz, R. L. 2004 [arXiv:astro-ph/0405087]
Chib, S., & Jeliazkov, I. 2001, JASA, 96, 270
CoRoT 2006, The CoRoT Mission, pre-launch status, ESA SP, 1306
Eggleton, P. P., Kiseleva, L. G., & Hut, P. 1998, ApJ, 499, 853
Endl, M., Kürster, M., & Els, S. 2000, A&A, 362, 585
Etzel, P. B. 1981, in Photometric and Spectroscopic Binary Systems, ed. E. B. Carling, & Z. Kopal, 111
Ferraz-Mello, S., Rodríguez, A., & Hussmann, H. 2008, Cel. Mech. Dyn. Astron., 101, 171
Fitzpatrick, E. L. 1999, PASP, 111, 63
Gandolfi, D., Alcalá, J. M., Leccia, S., et al. 2008, ApJ, 687, 1303
Gillon, M., Hatzes, A., Csizmadia, S., et al. 2010, A&A, 520, A97
Girardi, L., Williams, B. F., Gilbert, K. M., et al. 2010, ApJ, 724, 1030
Giuppone, C. A., Tadeu dos Santos, M., Beaugé, C., Ferraz-Mello, S., & Michtchenko, T. A. 2009, ApJ, 699, 1321
Guillot, T. 2005, Ann. Rev. Earth Planet. Sci., 33, 493
Guillot, T. 2008, Physica Scripta Volume T, 130, 014023
Guillot, T., & Havel, M. 2011, A&A, 527, A20
Guillot, T., & Morel, P. 1995, A&AS, 109, 109
Hansen, B. M. S. 2010, ApJ, 723, 285
Havel, M., Guillot, T., Valencia, D., & Crida, A. 2011, A&A, 531, A3
Hut, P. 1981, A&A, 99, 126
Ikoma, M., Guillot, T., Genda, H., Tanigawa, T., & Ida, S. 2006, ApJ, 650, 1150
Jeffreys, H. 1961, The Theory of Probability, Oxford
Lainey, V., Arlot, J.-E., Karatekin, Ö., & van Hoolst, T. 2009, Nature, 459, 957
Malmberg, D., & Davies, M. B. 2009, MNRAS, 394, L26
Marigo, P., Girardi, L., Bressan, A., et al. 2008, A&A, 482, 883
Mayor, M., Pepe, F., Queloz, D., et al. 2003, The Messenger, 114, 20
Mignard, F. 1979, Moon and Planets, 20, 301
Morel, P., & Lebreton, Y. 2008, Ap&SS, 316, 61
Ogilvie, G. I., & Lin, D. N. C. 2004, ApJ, 610, 477
Papaloizou, J. C. B., & Terquem, C. 2006, Rep. Progr. Phys., 69, 119
Pepe, F., Mayor, M., Galland, F., et al. 2002a, A&A, 388, 632
Pepe, F., Mayor, M., Rupprecht, G., et al. 2002b, The Messenger, 110, 9
Perna, R., Menou, K., & Rauscher, E. 2010, ApJ, 719, 1421
Popper, D. M., & Etzel, P. B. 1981, AJ, 86, 102
Reid, I. N., Brewer, C., Brucato, R. J., et al. 1991, PASP, 103, 661
Sing, D. K. 2010, A&A, 510, A21
Skrutskie, M. F., Cutri, R. M., Stiening, R., et al. 2006, AJ, 131, 1163
Southworth, J., Maxted, P. F. L., & Smalley, B. 2004a, MNRAS, 351, 1277
Southworth, J., Zucker, S., Maxted, P. F. L., & Smalley, B. 2004b, MNRAS, 355, 986
Torres, G., Konacki, M., Sasselov, D. D., & Jha, S. 2005, ApJ, 619, 558
Torres, G., Andersen, J., & Giménez, A. 2010, A&ARv, 18, 67
Torres, G., Fressin, F., Batalha, N. M., et al. 2011, ApJ, 727, 24
Wuchterl, G. 2011, in The Astrophysics of Planetary Systems: Formation, Structure, and Dynamical Evolution, ed. A. Sozzetti, M. G. Lattanzi, & A. P. Boss, IAU Symp., 276, 76
Zakamska, N. L., Pan, M., & Ford, E. B. 2011, MNRAS, 410, 1895

[1] Institut d'astrophysique spatiale, Université Paris-Sud 11 & CNRS (UMR 8617), Bât. 121, 91405 Orsay, France
e-mail: marc.ollivier@ias.u-psud.fr
[2] IAG, Université de Liège, Allée du 6 août 17, Liège 1, Belgium

[3] Laboratoire d'Astrophysique de Marseille – LAM, Université d'Aix-Marseille & CNRS, UMR 7326, 38 rue F. Joliot-Curie, 13388 Marseille Cedex 13, France
[4] Thüringer Landessternwarte, 07778 Tautenburg, Germany
[5] Université de Nice-Sophia Antipolis, CNRS UMR 6202, Observatoire de la Côte d'Azur, BP 4229, 06304 Nice Cedex 4, France
[6] Department of Physics and AstronomyAarhus University, 8000 Aarhus C, Denmark
[7] Institute of Planetary Research, German Aerospace Center, Rutherfordstrasse 2, 12489 Berlin, Germany
[8] McDonald Observatory, University of Texas at Austin, Austin, 78712 TX, USA
[9] Research and Scientific Support Department, European Space Agency, Keplerlaan, 2200 AG Noordwijk, The Netherlands
[10] Department of Physics, Denys Wilkinson Building Keble Road, Oxford, OX1 3RH, UK
[11] Instituto de Astrofísica de Canarias, 38205 La Laguna, Tenerife, Spain
[12] Departamento de Astrofísica, Universidad de La Laguna, 38200 La Laguna, Tenerife, Spain
[13] Observatoire de Genève, Université de Genève, 51 Ch. des Maillettes, 1290 Sauverny, Switzerland
[14] LESIA, UMR 8109 CNRS, Observatoire de Paris, UVSQ, Université Paris-Diderot, 5 place J. Janssen, 92195 Meudon, France
[15] Institut d'astrophysique de Paris, Université Paris 6 & CNRS (UMR 7095), 98 bd Arago, 75014 Paris, France
[16] Observatoire de Haute-Provence, CNRS & OAMP, 04870 St-Michel l'Observatoire, France
[17] Rheinisches Institut für Umweltforschung an der Universität zu Köln, Aachener Str. 209, 50931 Köln, Germany
[18] Institute for Astronomy, University of Vienna, Türkenschanzstrasse 17, 1180 Vienna, Austria
[19] Institute of Astronomy, Geophysics and Atmospheric Sciences, University of São Paulo, Brasil
[20] Space Research Institute, Austrian Academy of Sciences, Schmiedlstr. 6, Graz, Austria
[21] Wise Observatory, Tel Aviv University, 69978 Tel Aviv, Israel
[22] Center for Astronomy and Astrophysics, TU Berlin, Hardenbergstrasse 36, 10623 Berlin, Germany
[23] Laboratoire de l'univers et de ses théories, Observatoire de Paris & CNRS (UMR 8102), 5 place Jules Janssen, 92195 Meudon, France